ADVANCED MATERIALS
www.advmat.de

Check for updates

Highly Efficient 2D/3D Hybrid Perovskite Solar Cells via Low-Pressure Vapor-Assisted Solution Process

Ming-Hsien Li, Hung-Hsiang Yeh, Yu-Hsien Chiang, U-Ser Jeng, Chun-Jen Su, Hung-Wei Shiu, Yao-Jane Hsu, Nobuhiro Kosugi, Takuji Ohigashi, Yu-An Chen, Po-Shen Shen, Peter Chen, and Tzung-Fang Guo**

The fabrication of multidimensional organometallic halide perovskite via a low-pressure vapor-assisted solution process is demonstrated for the first time. Phenyl ethyl-ammonium iodide (PEAI)-doped lead iodide (PbI_2) is first spin-coated onto the substrate and subsequently reacts with methyl-ammonium iodide (MAI) vapor in a low-pressure heating oven. The doping ratio of PEAI in MAI-vapor-treated perovskite has significant impact on the crystalline structure, surface morphology, grain size, UV–vis absorption and photoluminescence spectra, and the resultant device performance. Multiple photoluminescence spectra are observed in the perovskite film starting with high PEAI/PbI_2 ratio, which suggests the coexistence of low-dimensional perovskite ($PEA_2MA_{n-1}Pb_nI_{3n+1}$) with various values of *n* after vapor reaction. The dimensionality of the as-fabricated perovskite film reveals an evolution from 2D, hybrid 2D/3D to 3D structure when the doping level of PEAI/PbI_2 ratio varies from 2 to 0. Scanning electron microscopy images and Kelvin probe force microscopy mapping show that the PEAI-containing perovskite grain is presumably formed around the $MAPbI_3$ perovskite grain to benefit $MAPbI_3$ grain growth. The device employing perovskite with PEAI/PbI_2 = 0.05 achieves a champion power conversion efficiency of 19.10% with an open-circuit voltage of 1.08 V, a current density of 21.91 mA cm^{-2}, and a remarkable fill factor of 80.36%.

Organic–inorganic hybrid perovskite materials have attracted numerous attentions in solar energy conversion and various optoelectronic applications[1] due to their long carrier diffusion length, high absorption coefficients in the visible range, and high carrier mobility.[2,3] A typical perovskite has a 3D lattice structure with a formula of ABX_3 where A^+ is composed of organic ($CH_3NH_3^+$ (MA^+) or $CH_3(NH_2)_2^+$ (FA^+)) or inorganic (cesium$^+$ (Cs^+) or rubidium$^+$ (Rb^+)) cation, B^{2+} is the divalent metal (Pb^{2+} or Sn^{2+}), and X^- is the halide (Cl^-, Br^-, or I^-).[2,4] To realize commercial applications, the long-term stability issues such as durability under humid, thermal, and light-soaking conditions should be further investigated and improved.[5] Most annoyingly, the perovskite thin film is quite sensitive to moisture and oxygen, resulting in degradation under atmosphere. The low formation energy of the perovskite structures tends to hydrolyze in the presence of moisture.[6] One of the methods to stabilize halide perovskite is to use the layered structure with 2D perovskites, the so-called Ruddlesden–Popper layered perovskites, where larger hydrophobic cation acts as a spacer to isolate the 3D $MAPbI_3$.[7–12] The general formula of Ruddlesden–Popper perovskites is defined as $A'_2A_{n-1}B_nX_{3n+1}$, where *n* is an integer between 1 and ∞ and A'^+ is large-sized cation (typically ammonium-based cation such as phenyl ethylammonium (PEA),[10] polyethylenimine (PEI),[13] *n*-butylammine (BA),[14] cyclopropylamine (CA),[15] octadecylamine (OA),[16] or ammoniumvaleric

Dr. M.-H. Li, H.-H. Yeh, Y.-H. Chiang, Y.-A. Chen, P.-S. Shen, Prof. P. Chen, Prof. T.-F. Guo
Department of Photonics
National Cheng Kung University
Tainan 701, Taiwan
E-mail: petercyc@mail.ncku.edu.tw; guotf@mail.ncku.edu.tw
Prof. U. Jeng, Dr. C.-J. Su, Dr. H.-W. Shiu, Dr. Y.-J. Hsu
National Synchrotron Radiation Research Center
Hsinchu 300, Taiwan
Prof. U. Jeng
Department of Chemical Engineering
National Tsing Hua University
Hsinchu 30013, Taiwan
Prof. N. Kosugi, Dr. T. Ohigashi
UVSOR Synchrotron
Institute for Molecular Science
Myodaiji, Okazaki 444-8585, Japan
Prof. P. Chen
Center for Micro/Nano Science and Technology (CMNST)
National Cheng Kung University
Tainan 701, Taiwan
Prof. P. Chen
Hierarchical Green-Energy Materials (Hi-GEM) Research Center
National Cheng Kung University
Tainan 701, Taiwan
The ORCID identification number(s) for the author(s) of this article can be found under https://doi.org/10.1002/adma.201801401.

DOI: 10.1002/adma.201801401

© 2018 WILEY-VCH Verlag GmbH & Co. KGaA, Weinheim

acid (AVA)[17,18]) which is not compatible with ABX_3 lattice structure. Smith et al. synthesized $(PEA)_2(MA)_2Pb_3I_{10}$ perovskite as light absorber for the planar perovskite solar cells (PSCs) with a remarkable open-circuit voltage (V_{OC}) of 1.18 V. The large organic group intercalation into the 3D perovskite structure increases the bandgap as well as the device V_{OC} due to the reduced dimensionality. However, its insulating nature leads to quantum confinement effect that limits charge transport in 2D perovskites and the resultant short-circuit current density (J_{SC}). Notably, the $(PEA)_2(MA)_2Pb_3I_{10}$ perovskite maintains stable perovskite structure for 46 days under air environment with 52% relative humidity.[10] Gan et al. applied one-step spin-coating to fabricate 2D $(PEA)_2(MA)_{n-1}Pb_nI_{3n+1}$ perovskite solar cells with $n = 1$, 2, and 3, in which the TiO_2-nanorod-based device made with $n = 3$ perovskite exhibited hybrid phase (multi n value in the perovskite film) and the best performance of 3.72%. All the deposited perovskite films remained unchanged after 60 days as exposure to relative humidity of 60%.[8] Quan et al. proposed to increase the $MAPbI_3$ interlayer number and synthesized quasi-2D $(PEA)_2(MA)_{n-1}Pb_nI_{3n+1}$ perovskite with the n value from 1 to ∞. The best-performing device achieved an impressive efficiency of 15.36% with a notable V_{OC} of 1.09 V for $n = 60$ and superior stability than the 3D $MAPbI_3$ counterpart.[19] Similarly, Cohen et al. prepared the PSCs employing quasi-2D $(PEA)_2(MA)_{n-1}Pb_nBr_{3n+1}$ perovskite with high n value of 50 to obtain an efficiency of 8.5% with an impressive V_{OC} of 1.46 V.[20] Grancini et al. reported an ultrastable 2D/3D perovskite by mixing AVAI, methyl-ammonium iodide (MAI), and inorganic PbI_2. They achieved 14.6% efficiency for PSCs and demonstrated extraordinary long-term stability over 5000 h in 10 × 10 cm^2 hole-conductor free large area modules.[12,17] Cao et al. prepared one-step spin-coated $(BA)_2(MA)_{n-1}Pb_nI_{3n+1}$ for perovskite solar cells with n = 1, 2, 3, and 4, among which the layer orientation of $(BA)_2(MA)_2Pb_3I_{10}$ is out-of-plane to facilitate carrier transport and the device showed an efficiency of 4.02%.[21] Jung prepared 2D-perovskite-based solar cells with power conversion efficiency (PCE) of 5.43% via MAI vapor reaction with BA_2PbI_4 film under atmospheric pressure.[11] Stoumpos et al. synthesized pure 2D phase $(BA)_2(MA)_4Pb_5I_{16}$ perovskite using hot-casting assisted solution process. The planar p–i–n inverted device with $n = 5$ demonstrated an excellent efficiency of 8.71%.[9] A great success had been made by Tsai et al. who employed hot-casting process to well-control the crystal orientation of 2D $(BA)_2(MA)_3Pb_4I_{13}$ film. An enhanced efficiency of 12.52% with improved humidity resistance was achieved for the solar cells due to the out-of-plane orientation that facilitated the charge extraction by the selective contact.[22] Zhang et al. introduced Cs^+ in the 2D $(BA)_2(MA)_3Pb_4I_{13}$ to further stabilize the 3D $MAPbI_3$ lattice structure and lower the trap-state density. The 2D Cs-doped $(BA)_2(MA)_3Pb_4I_{13}$-based perovskite solar cells delivered an impressive efficiency of 13.68% with improved moisture tolerance and thermal stability.[23] Wang et al. introduced BA^+ into mixed-cation lead mixed-halide $FA_{0.83}Cs_{0.17}Pb(I_yBr_{1-y})_3$ 3D perovskite to form 2D/3D heterostructure, in which the formations of 2D perovskite platelets grow across the substrate to intersperse between highly orientated 3D perovskite grains. The 2D perovskite platelets suppress nonradiative charge recombination resulting from the trap-state at grain boundary and enhance the film stability. The 2D/3D hybrid perovskite solar cells exhibit an impressive efficiency of 17.5 ± 1.3% with promising stability for 2400 h.[24] In addition to the large-sized organic cation stabilized organic–inorganic perovskite, intercalation of large-sized organic cation, such as BA^+ or EDA^{2+}, can further enhance the stability of all-inorganic $CsPbI_3$ perovskite.[25] Furthermore, a 2D perovskite covering on the 3D perovskite serves as an interfacial layer to protect the underlying 3D perovskite from the moisture penetration and effectively prolong device lifetime.[15,18,26]

The environment-friendly lead-free perovskites are recently synthesized by substituting the divalent Pb with Sn, Ge, Cu, Sb, or Bi,[27] among which tin-based perovskite is a promising alternative due to its superior optical and electrical properties than others. Several Sn-based low-dimensional perovskite-based solar cells have been developed by solution process with PCE lower than 10%.[28–30]

Vapor-based deposition has been demonstrated as a promising approach for fabrication of high quality and large-scale perovskite active area in virtue of well-controlled reaction rate.[31] Among the various proposed vapor deposition techniques, low-pressure vapor-assisted solution deposition method (LP-VASP) operated under low pressure provides advantages of faster vapor diffusion rate, lower sublimation temperature, and shorter reaction time for perovskite film growth. Thus, LP-VASP is a feasible route to obtain smooth, pinhole-free, highly uniform perovskite films.[32,33] Most of low-dimensional lead or lead-free halide perovskites are fabricated with solution process; nevertheless, the LP-VASP has not been applied to fabricate low-dimensional 2D or 2D/3D mixed perovskite.

Motivated from the published literatures, we employ LP-VASP to fabricate highly efficient 2D/3D perovskite solar cells. Various doping level of PEAI in the PbI_2 precursor along with different concentrations and reaction times are investigated for perovskite film preparation to optimize the device performance. The best performed device made with PEAI/PbI_2 = 0.05 (precursor ratio) demonstrates a V_{OC} of 1.08 V, J_{SC} of 21.91 mA cm^{-2}, and fill factor (FF) of 0.80, leading to a remarkable efficiency of 19.10%. The crystalline phases, morphologies, and optical absorption of perovskite film with variant doping levels are characterized by X-ray diffraction (XRD), grazing-incidence wide-angle X-ray scattering (GIWAXS), scanning electron microscopy (SEM), and UV–vis spectrometry, respectively. From these characteristics, we observe the dimensionality evolution from 2D, hybrid 2D/3D to 3D structure when the doping level of PEAI/PbI_2 varied from 2 to 0. For the champion performance of perovskite solar cells with the ratio of PEAI/PbI_2 = 0.05, the PEAI-intercalated perovskite prefers to form tiny island around matrix $MAPbI_3$ grain and facilitates the $MAPbI_3$ crystallization. The near edge X-ray absorption fine structure (NEXAFS) spectra and Kelvin probe force microscopy (KPFM) results verify that PEA^+ remains in the perovskite film and enhances the surface potential along with the V_{OC} for the perovskite solar cell with PEAI/PbI_2 = 0.05.

The perovskite film is prepared using LP-VASP by solid–vapor reaction between spin-coated PEAI-doped PbI_2 film (deposited on the mesoporous (mp)-TiO_2) and MAI vapor under controlled pressure, as reported in our previous works.[32,33] The reaction time for the chemical reaction of MAI vapor with PEAI-doped PbI_2 film is fixed to be 2 h. The

© 2018 WILEY-VCH Verlag GmbH & Co. KGaA, Weinheim

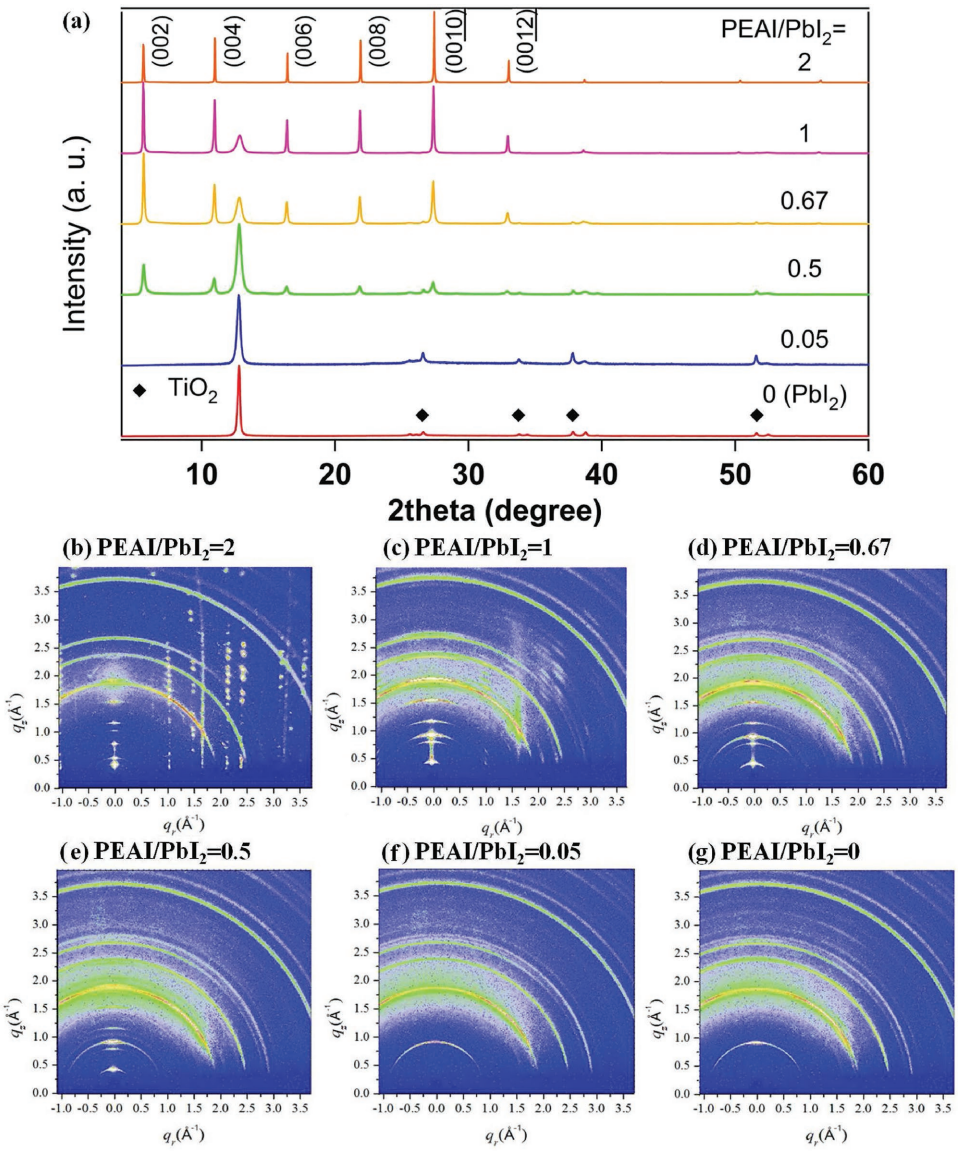

Figure 1. a) XRD of PEAI-doped PbI_2 film with PEAI/PbI_2 = 2, 1, 0.67, 0.5, and 0.05 on the mp-TiO_2 substrate, compared with that of the PbI_2 (PEAI/PbI_2 = 0). b–g) Corresponding GIWAXS patterns, with the scattering vector components in the out-of-plane and in-plane directions defined by q_z and q_r (detailed in the Supporting Information). Note that the powder ring pattern in (b) is attributed to mp-TiO_2 substrate layer (cf. Figure 3a), which is commonly observed in all other patterns.

doping level of PEAI with respect to (w.r.t) PbI_2 in molar ratio is varied as 2:1, 1:1, 1:1.5, 1:2, 1:10, 1:20, 1:30, 0 and denoted as PEAI/PbI_2 = 2, 1, 0.67, 0.5, 0.1, 0.05, 0.03, and 0 for convenience. XRD and GIWAXS[34,35] are employed to examine the crystalline textures of the perovskite film with different doping levels. **Figure 1**a presents the XRD profiles of PEAI-doped PbI_2 films deposited on the mp-TiO_2 substrate before vapor treatment with PEAI/PbI_2 = 2, 1, 0.67, 0.5, 0.05, and 0 (pure PbI_2). With the film made of PEAI/PbI_2 = 2, periodic peaks located at 5.5°, 11°, 16.6°, 22°, 27.5°, and 33° are observed and indexed as (002), (004), (006), (008), (00$\underline{10}$), and (00$\underline{12}$) of a layer structure stacked parallel to the substrate, revealing the 2D $(PEA)_2PbI_4$ perovskite. The corresponding layer spacing is 32.2 Å deduced from the peak positions. Increasing the molar ratio of PbI_2 of the films for PEAI/PbI_2 = 1, 0.67, 0.5, and 0.05 does not alter the layer structure (i.e., lamellar peak positions), but gives rise to the emergence and gradually enhanced feature (001) peak of PbI_2 crystals at $2\theta = 13°$. The result suggests that when the composition PEAI/PbI_2 is below 2, excess PbI_2 coexists with $(PEA)_2PbI_4$ crystals. Figure 1b–g shows the GIWAXS patterns for the PEAI-doped PbI_2 films with PEAI/PbI_2 = 2, 1, 0.67, 0.5, and 0.05 that are spin-coated on the mp-TiO_2 substrate without MAI vapor treatment, compared with that of neat PbI_2 (PEAI/PbI_2 = 0) film. In Figure 1b, the prominent powder-ring pattern is contributed by mp-TiO_2 (cf. Figure 3a). On top of that, the highly ordered diffraction spots on and off the meridian direction (z) (film surface normal) reveal a 2D-layered structure of $(PEAI)_2Pb_2I_4$. With increasingly larger PbI_2 content, the

© 2018 WILEY-VCH Verlag GmbH & Co. KGaA, Weinheim

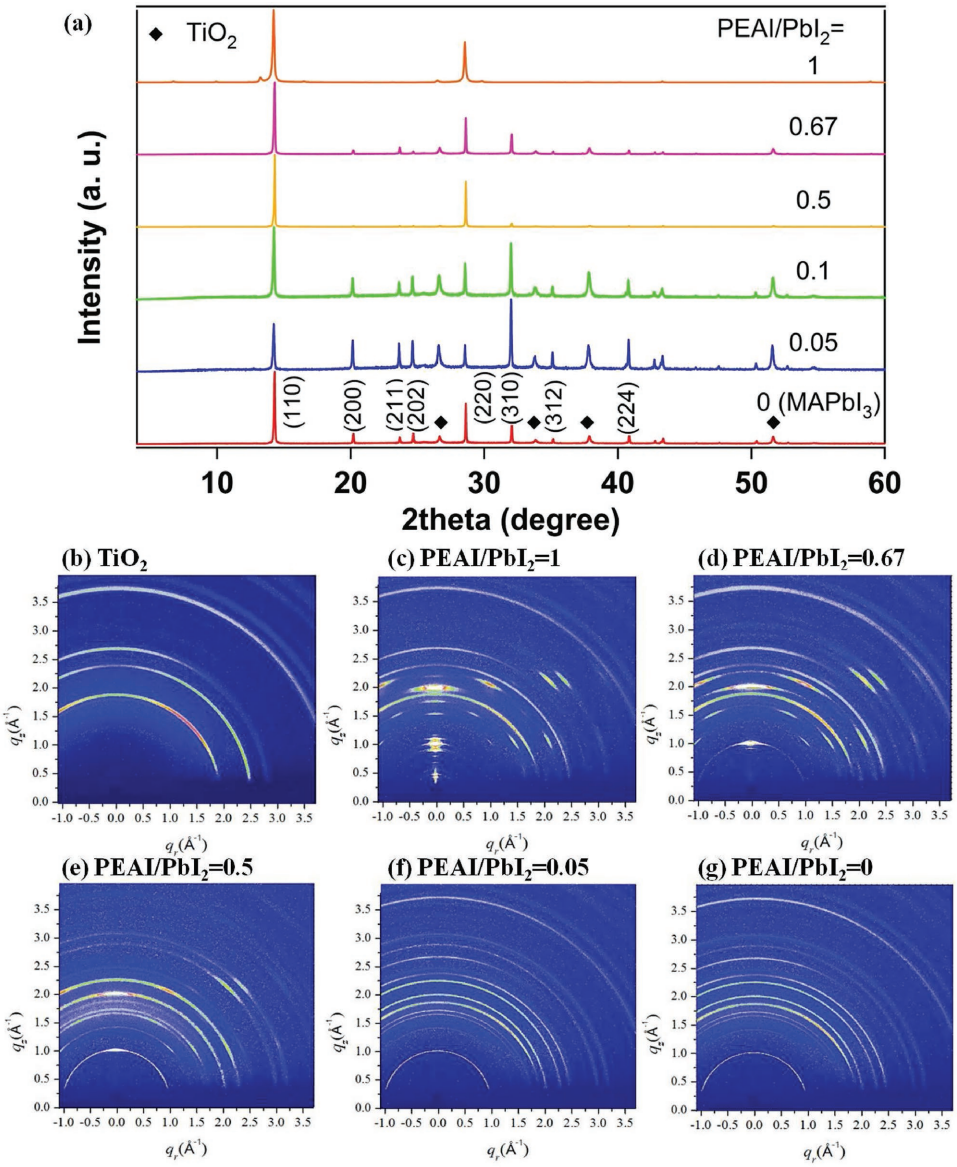

Figure 2. a) XRD of MAI-vapor-treated perovskite film with PEAI/PbI_2 = 1, 0.67, 0.5, 0.05, and 0 ($MAPbI_3$) that are covered on the mp-TiO_2 substrate. The characteristic peaks of mp-TiO_2 are marked by solid diamonds. b–g) The GIWAXS patterns of mp-TiO_2 (b), and PEAI-doped PbI_2 film with PEAI/PbI_2 = 1 (c), 0.67 (d), 0.5 (e), 0.05 (f), and 0 (g) ($MAPbI_3$) on the mp-TiO_2 substrate.

crystal deflection spots of $(PEAI)_2Pb_2I_4$ successively broaden and deteriorate (Figure 1c–e), and eventually diminish at PEAI/PbI_2 = 0.05 and 0 (Figure 1f,g). The deterioration of the oriented layering structure is accompanied by increasingly intensified powder rings of 3D randomly orientated PbI_2 crystals (Figure 1g). These results evidence that the PEAI-doped PbI_2 film structure can be modulated by the PEAI and PbI_2 ratio from pure 2D perovskite (PEAI/PbI_2 = 2) of prominent layering features, to coexisted 2D perovskite and PbI_2 hybrid crystals (PEAI/PbI_2 = 1, 0.67, and 0.5), and to neat PbI_2 crystals (PEAI/PbI_2 = 0.05 and 0).

Figure 2a displays the XRD profiles of the MAI-vapor-treated PEAI-doped PbI_2 films with PEAI/PbI_2 = 1, 0.67, 0.5, 0.1, 0.05, and 0, revealing successive phase transformations of multiphase perovskite into single-phase perovskite of $MAPbI_3$. It is worth noting that the XRD pattern in Figure 2a exhibits new order phases for the perovskite film prepared with PEAI/PbI_2 = 1. The corresponding XRD profile of Figure 2a in logarithmic scale is provided in Figure S1a (Supporting Information) to highlight the discrepancy of the perovskite film with variant doping levels, indicating that only perovskite film made of PEAI/PbI_2 = 1 could have other perovskite phases. The magnified peaks with logarithmic scale suggest that the other phases with limited domain size are residual in the final film. The possible phases in the final film of PEAI/PbI_2 = 1 deduced from the interlayer spacing are supposed to be $(PEA)_2PbI_4$, $(PEA)_2(MA)_1Pb_2I_7$, $(PEA)_2(MA)_2Pb_3I_{10}$, and $(PEA)_2(MA)_4Pb_5I_{16}$ 2D perovskite members, as depicted in Figure S1b (Supporting Information). These new order phases presumably transform from the 2D $(PEA)_2PbI_4$ perovskite after MAI vapor reaction.

© 2018 WILEY-VCH Verlag GmbH & Co. KGaA, Weinheim

Owing to the weak van der Waals interaction between the organic PEA^+ cation and the inorganic octahedral PbI_6,[11] the vapor MA^+ cation accessibly intercalates into the octahedral PbI_6 to form 2D perovskite. With increasing PbI_2 content for $PEAI/PbI_2 = 0.67$, 0.5, 0.1, 0.05, and 0, the new ordered phases vanish, while the feature peaks of 3D $MAPbI_3$ prevail as the predominant phase in the vapor-treated film. We further examine the XRD profiles of spin-coated films for overdosing cases of $PEAI/PbI_2 = 3$ and 4 and their counterparts after vapor treatment, as depicted in Figure S1c (Supporting Information). The as-deposited films without vapor reaction exhibit two characteristic peaks series, among which one is $(PEA)_2PbI_4$ (00*l*) facets and the other is supposed to be $(PEA)_2PbI_4$ (*nml*) facets. After vapor treatment, the marked peaks are presumably responsible for the 2D perovskites of $(PEA)_2PbI_4$, $(PEA)_2(MA)_1Pb_2I_7$, $(PEA)_2(MA)_2Pb_3I_{10}$, and $(PEA)_2(MA)_4Pb_5I_{16}$. Our results suggest that the multi-2D perovskite phases coexist with 3D $MAPbI_3$ perovskite in the MAI-treated films when the doping level of $PEAI/PbI_2$ exceeds 1.

The GIWAXS patterns of mp-TiO_2 substrate and the PEAI-doped PbI_2 films with $PEAI/PbI_2 = 1$, 0.67, 0.5, 0.05, and 0 after MAI vapor reaction are presented in Figure 2b–g, revealing successive crystal orientation of the as-fabricated perovskite film. The $PEAI/PbI_2 = 1$ sample exhibits a new ordered diffraction spot on the meridian direction in Figure 2c ($q_z < 1.2$ Å^{-1}), which corresponds to the 2D $(PEA)_2(MA)_4Pb_5I_{16}$ phase. The diffraction spots off the meridian direction are ascribed to the $MAPbI_3$ crystals whose indexes are labeled in Figure S2a (Supporting Information). The results also indicate that 2D-layered and 3D $MAPbI_3$ perovskite coexist in the vapor-treated film, among which $MAPbI_3$ perovskite exhibits specific orientation. With increasing PbI_2 content ($PEAI/PbI_2 = 0.67$, 0.5, 0.05, and 0), the new ordered diffraction spots vanish, while the diffraction spots of $MAPbI_3$ successively broaden for $PEAI/PbI_2 = 0.67$ and 0.5 (Figure 2d,e) and eventually form powder rings for $PEAI/PbI_2 = 0.05$ and 0 (Figure 2f,g). Increasing the molar ratio of PbI_2 increases 3D $MAPbI_3$ domain accompanied with random orientation and deteriorates 2D perovskite phases. Figure S2c (Supporting Information) shows the integrated intensity profiles from GIWAXS for perovskite films made of $PEAI/PbI_2 = 1$, 0.67, and 0.5 compared with that of $PEAI/PbI_2 = 1$ without vapor treatment. For the $PEAI/PbI_2 = 1$ sample before vapor treatment (black line), the main phases after spin-coating are composed of PbI_2 and $(PEA)_2PbI_4$ whose index is labeled as (00*l*). After vapor reaction (red dashed line in Figure S2c in the Supporting Information), partial PbI_2 converts into $MAPbI_3$ perovskite with characteristic peaks corresponding to $(110)_P$, $(220)_P$, and $(310)_P$, while partial $(PEA)_2PbI_4$ transforms to the layered structure of $(PEA)_2(MA)_4Pb_5I_{16}$ perovskite denoted as (00*l*)′ in Figure S2c (Supporting Information). Hence, multiple phases of PbI_2, $MAPbI_3$, $(PEA)_2PbI_4$, and $(PEA)_2(MA)_4Pb_5I_{16}$ are observed in the GIWAXS profile for the $PEAI/PbI_2 = 1$ sample after vapor reaction. As we have observed in Figure S1b (Supporting Information), $MAPbI_3$ and $(PEA)_2(MA)_4Pb_5I_{16}$ have more significant diffraction intensity in the logarithm plot. For those samples with less PEAI content like $PEAI/PbI_2 = 0.67$ (or 0.5), the $(110)_P$ peak of $MAPbI_3$ perovskite intensifies gradually, accompanied with significantly reduced feature peaks from residual PbI_2, $(PEA)_2PbI_4$, or layered $(PEA)_2(MA)_4Pb_5I_{16}$ perovskite. Consequently, as we increase the amount of PbI_2 in the solution precursor, the predominated phase in the vapor-treated film is $MAPbI_3$ perovskite, similar to what we observed in the XRD profiles. $MAPbI_3$ perovskite crystals can be gradually increased with decreasing $PEAI/PbI_2$ ratio, as shown in Figure S2d (Supporting Information). The results suggest that a small $PEAI/PbI_2$ ratio is advantageous in assisting the growth of the $MAPbI_3$ perovskite crystal and improving film morphology.[34]

Figure 3 shows the UV–vis absorption and photoluminescence (PL) spectra of the vapor-treated perovskite films formed on the mp-TiO_2 layer for $PEAI/PbI_2 = 1$, 0.67, 0.5, 0.1, 0.05, and 0.03 along with pure 2D ($PEAI/PbI_2 = 2$, $(PEA)_2PbI_4$, without vapor treatment) and 3D ($PEAI/PbI_2 = 0$, $MAPbI_3$) perovskite for comparison. Without the MAI vapor treatment, an absorption stopband at 540 nm along with a remarkable peak at 510 nm is detected for $PEAI/PbI_2 = 2$, among which the stable exciton transition at 510 nm evidences the presence of 2D layer structure.[8] Higher exciton binding energy for layered structure hinders the electron–hole pair separation, which results in stable excitation transition and extremely high PL intensity, as shown in Figure 3b. After the MAI vapor reaction, all the PEAI-doped perovskite films show similar absorption stopband at ≈780 nm which is close to that of $MAPbI_3$, as depicted in Figure 3a, suggesting that the predominant structure of MAI-vapor-treated perovskite is the 3D $MAPbI_3$. Notably, an exciton absorption peak at 610 nm is observed for $PEAI/PbI_2 = 1$ sample, which presumably results from the 2D $(PEA)_2(MA)_2Pb_3I_{10}$ structure. Figure S2b (Supporting Information) presents the revolution of the UV–vis absorption spectra for the perovskite film made of $PEAI/PbI_2 = 1$ with vapor reaction time of 0.5, 1, 2 h, revealing that the volume ratio of 2D and 3D perovskites changed with the reaction time. It is clear that two feature exciton absorption peaks around 510 and 610 nm and an absorption onset at ≈780 nm are simultaneously observed for the reaction time of 0.5 h. When the reaction time prolongs to 1 and 2 h, the characteristic peak of 510 nm merges in the base absorption of 3D $MAPbI_3$ due to increasing ratio of 2D perovskite transformation into 3D $MAPbI_3$ perovskite. It is noted that the resultant PL spectra for the perovskite made of $PEAI/PbI_2 = 1$ display not only a dominant peak around 780 nm but also subpeaks located at 537, 579, and 621 nm. The subpeaks at 537, 579, and 621 nm have been identified by single crystal of $(PEA)_2PbI_4$, $(PEA)_2(MA)_1Pb_2I_7$, and $(PEA)_2(MA)_2Pb_3I_{10}$ structures from the literature, respectively.[36] The dominant peak (at 780 nm) is contributed from the 3D $MAPbI_3$ perovskite, whereas three subpeaks are contributed from the 2D perovskite of $(PEA)_2PbI_4$, $(PEA)_2(MA)_1Pb_2I_7$, and $(PEA)_2(MA)_2Pb_3I_{10}$, as illustrated in the magnified PL spectra (cf. Figure 3c). These results evidenced that the vapor-treated perovskite film is composed of mixed 2D/3D hybrid dimensionality and corresponded well with our material characterization from XRD technique. The shoulder PL peak at ≈650 nm should be responsible for the $(PEA)_2(MA)_4Pb_5I_{16}$ perovskite; however, its PL intensity may be quenched by the main structure of 3D $MAPbI_3$ presumably due to the electron transfer to lower bandgap of $MAPbI_3$. We further compare the PL spectra with the perovskite films made of $PEAI/PbI_2 = 3$ and 4, as depicted in Figure 3c. Owing to the coexisted $(PEA)_2PbI_4$, $(PEA)_2(MA)_1Pb_2I_7$, $(PEA)_2(MA)_2Pb_3I_{10}$, and $(PEA)_2(MA)_4Pb_5I_{16}$ 2D perovskite phases, the corresponding

© 2018 WILEY-VCH Verlag GmbH & Co. KGaA, Weinheim

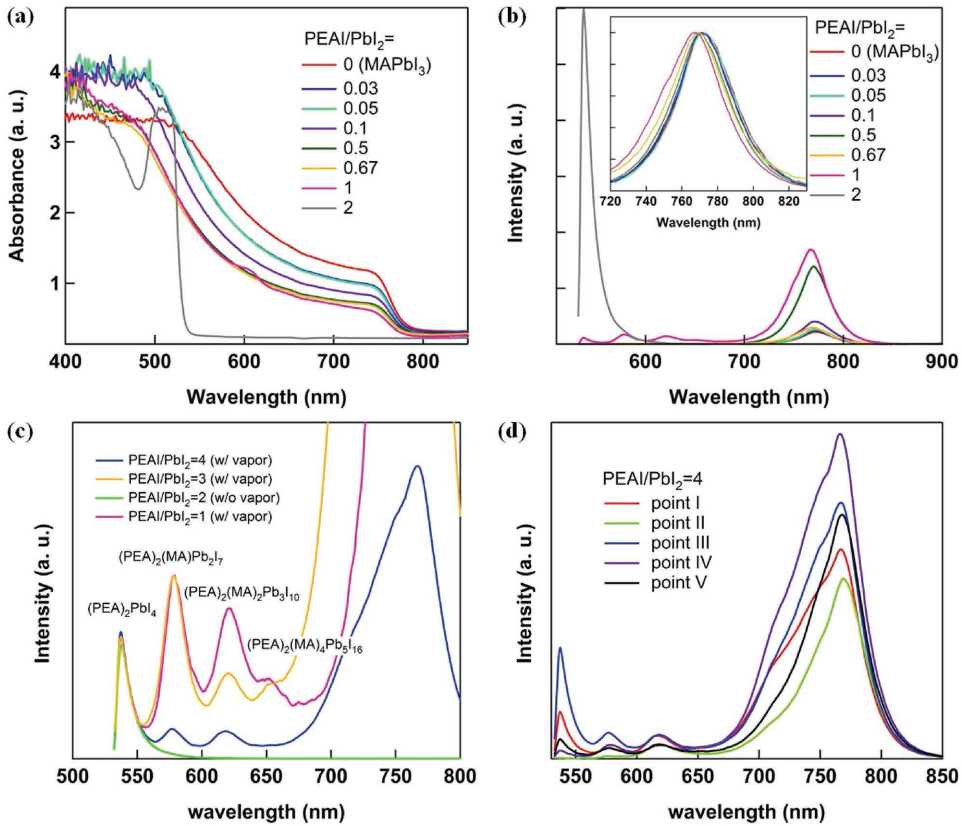

Figure 3. a,b) The UV–vis (a) and photoluminescence (PL) (b) spectra of perovskite with $PEAI/PbI_2$ = 2, 1, 0.67, 0.5, 0.1, 0.05, 0.03, and 0. The inset in (b) shows the normalized PL at ≈780 nm. c) The magnified PL spectra of vapor-treated film of $PEAI/PbI_2$ = 1, 3, and 4 compared with that of $PEAI/PbI_2$ = 2 (w/o vapor). d) The PL spectra of vapor-treated perovskite film with $PEAI/PbI_2$ = 4 pumped with variant positions.

PL spectra are similar to that of $PEAI/PbI_2$ = 1. Moreover, the position-dependent PL spectra of perovskite film with $PEAI/PbI_2$ = 4 shown in Figure 3d indicate the multi-2D perovskite randomly distributed in the film. No extra absorption and PL peaks are detected for further reducing PEAI amount of $PEAI/PbI_2$ = 0.67 and 0.5. With further increasing the content of PbI_2 for $PEAI/PbI_2$ = 0.1, 0.05, and 0.03, the vapor-treated perovskite films only present a dominant PL peak around 780 nm. The normalized PL signal insetted in Figure 3b reveals a blueshift with increasing the PEAI amount. The tiny shift of characteristic PL peak implies that the PEAI might act as an additive, as reported in previous works[9,37] or the PEAI intercalates into the $MAPbI_3$ to form a 2D $(PEA)_2(MA)_{n-1}Pb_nI_{3n+1}$ perovskite with a very large n value.

Furthermore, we examine the surface morphology of perovskite films with variant doping levels by SEM. Figure S3 (Supporting Information) presents the spin-coated film with different doping levels before vapor reaction. The self-intercalated 2D $(PEA)_2Pb_1I_4$ perovskite with $PEAI/PbI_2$ = 2 displays polycrystalline grains composed of large grain (over 1 µm) and interconnected network that fully cover onto the mp-TiO_2 substrate (cf. Figure S3a,b in the Supporting Information). With increasing the content of PbI_2 for $PEAI/PbI_2$ = 1, two phase domains are observed in the deposited film that are supposed to be the PbI_2 and $(PEA)_2PbI_4$ structure (cf. Figure S3c in the Supporting Information). The grain-like morphology might be resulted from the $(PEA)_2PbI_4$, while PbI_2 is phase-separated from the $(PEA)_2PbI_4$ grain with an interconnected feature. Further reducing the content of PEAI in the precursor for $PEAI/PbI_2$ = 0.2, 0.05, and 0, the surface morphology of spin-coated film is mainly dominated by the interconnected network of PbI_2, whereas the $(PEA)_2PbI_4$ domain is hardly observed (cf. Figure S3d–f in the Supporting Information). After MAI vapor reaction, the perovskite film with $PEAI/PbI_2$ = 1 reveals two phase domains of 2D perovskite and $MAPbI_3$ nanoplate which are, respectively, transformed from $(PEA)_2PbI_4$ and PbI_2, as seen in **Figure 4**a. With increasing the amount of PbI_2, the $MAPbI_3$ nanoplate grows to form $MAPbI_3$ grain (marked by blue circle in Figure 4b) for $PEAI/PbI_2$ = 0.67, multiple $MAPbI_3$ grain for $PEAI/PbI_2$ = 0.5 (cf. Figure 4c), and densely packed $MAPbI_3$ grain for $PEAI/PbI_2$ = 0.05, 0.03, and 0 (cf. Figure 4d–f). The morphology evolution is corresponding with the transformation of GIWAXS patterns which delivers an evolution from separately diffraction spots (specific orientation of $MAPbI_3$ nanoplate), broadened spots (multiorientation of $MAPbI_3$ grains) to powder rings (random orientation of densely packed $MAPbI_3$ grain). It is worth noting that the $MAPbI_3$ grains gradually grow with the decrease of PEAI content and accompanied with tiny island separated around the grain boundary that is marked by red circle in Figure 4c,d. For the $PEAI/PbI_2$ ratio of 0.05, the $MAPbI_3$ grain size is enhanced as compared to $PEAI/PbI_2$ = 0.03 and 0 (pure $MAPbI_3$). The

© 2018 WILEY-VCH Verlag GmbH & Co. KGaA, Weinheim

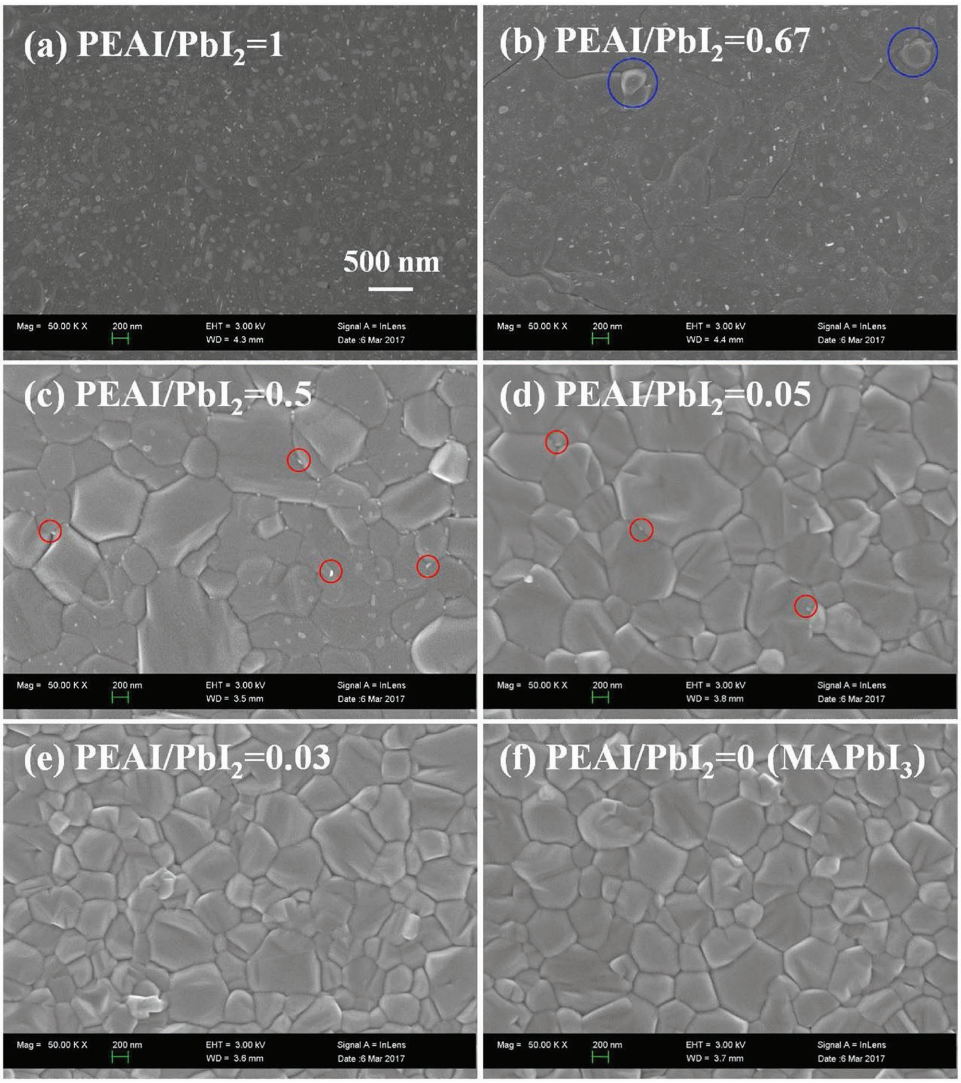

Figure 4. Top-view SEM images of vapor-treated perovskite film with PEAI/PbI_2 = 1 (a), 0.67 (b), 0.5 (c), 0.05 (d), 0.03 (e), and 0 (f) ($MAPbI_3$). The scale bar is 500 nm.

tendency of coarsening $MAPbI_3$ crystallinity as a function of PEAI/PbI_2 ratio is consistent with the GISAXS results in Figure S2d (Supporting Information). Further, the SEM morphology evolution implies that tiny island is presumably consisted of PEAI-intercalated perovskite and appropriate doping of PEAI improves the $MAPbI_3$ grain size.

We further conduct KPFM to realize the impact of PEA^+ on the surface potential of the as-fabricated film. **Figure 5**a–c presents the surface potential mapping of perovskite film made of PEAI/PbI_2 = 2 ($(PEA)_2PbI_4$), PEAI/PbI_2 = 0.05 (with MAI vapor treatment), and PEAI/PbI_2 = 0 ($MAPbI_3$) within 5 × 5 μm^2 scanning area. As expected, the 2D-layered $(PEA)_2PbI_4$ exhibits higher potential than the $MAPbI_3$ counterpart due to the reduced dimensionality. It is noted that the blue spots are responsible for the discontinuity of surface morphology, as seen in Figure S3a (Supporting Information). With tiny amount of PEA^+ doped in the $MAPbI_3$ perovskite film for PEAI/PbI_2 = 0.05, the surface potential is slightly increased (≈20 mV) than the $MAPbI_3$ perovskite. Figure 5d–f illustrates the correlation between surface potential and surface morphology for these samples by overlapping their images together. It is noted that, in Figure 5e, a higher surface potential pinpoints the tiny island around the grain boundary as we observe in the SEM images (cf. Figure 4d). A slightly increased surface potential also suggests the high *n*-member $(PEA)_2(MA)_{n-1}Pb_nI_{3n+1}$ within the tiny island. In contrast to pure $MAPbI_3$, more uniform distributed surface potential without remarkable spot is detected, as seen in Figure 5f.

Scheme 1 summaries the dimensionality evolution of MAI-vapor-treated perovskite film with variant doping levels of PEAI/PbI_2 that are transformed from the solution-processed film on the mp-TiO_2 substrate. Before the MAI vapor reaction, the self-intercalated $(PEA)_2Pb_1I_4$ 2D perovskite is phase-separated from the PbI_2 matrix in the film of PEAI/PbI_2 = 1. With increasing the amount of PbI_2 for PEAI/PbI_2 < 1, the 2D $(PEA)_2Pb_1I_4$ domain residual in the film gradually diminishes

© 2018 WILEY-VCH Verlag GmbH & Co. KGaA, Weinheim

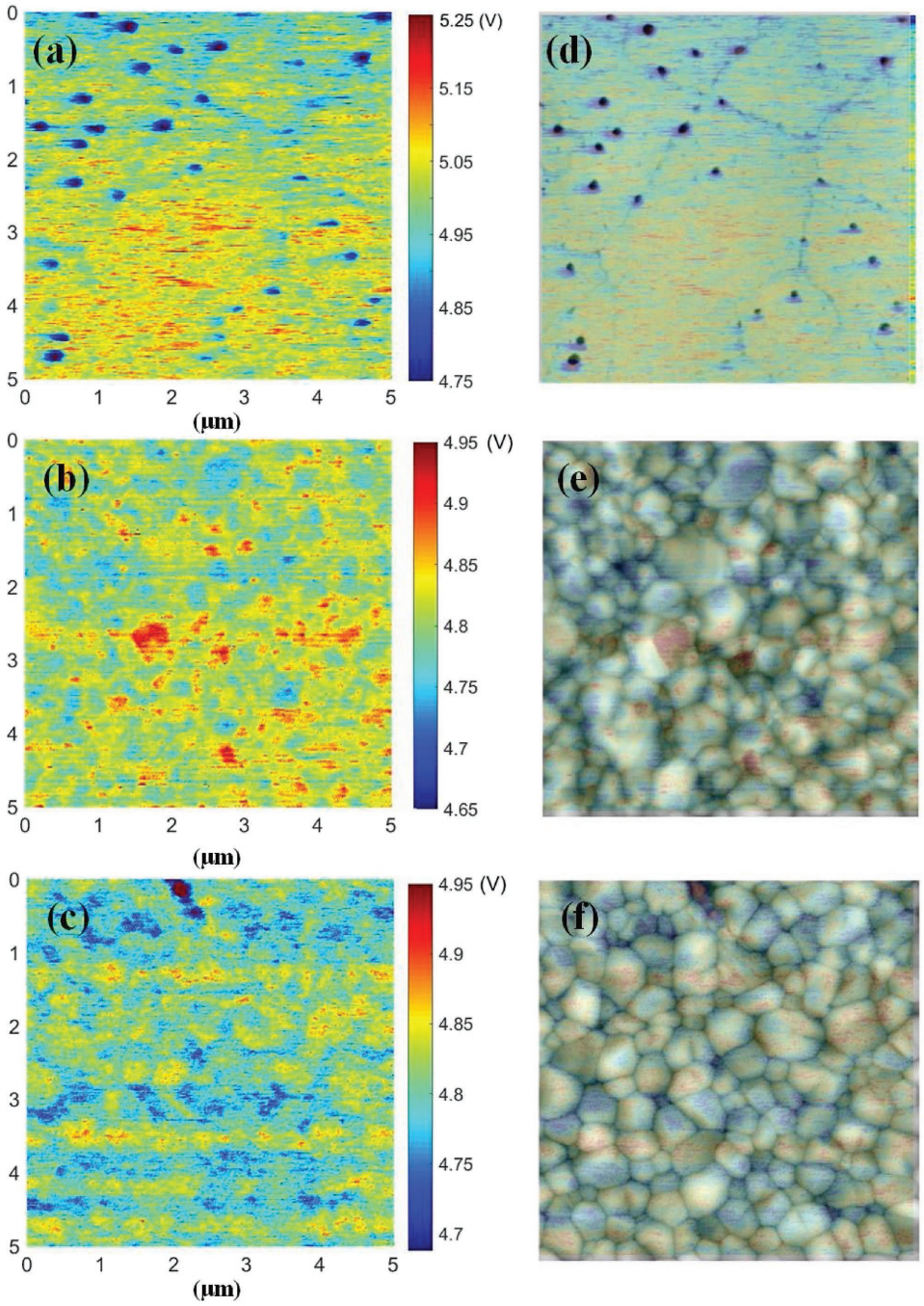

Figure 5. a–d) The surface potential and corresponding morphology mapping of perovskite film made of PEAI/PbI_2 = 2 (a,d), PEAI/PbI_2 = 0.05 (with vapor treatment) (b,e) and PEAI/PbI_2 = 0 ($MAPbI_3$) (c,f) with a scanning area of 5 μm × 5 μm. These samples are covered on FTO substrate coated with mp-Al_2O_3.

and vanishes for PEAI/PbI_2 = 0. After the PEA-doped PbI_2 film reacts with MAI vapor, $(PEA)_2Pb_1I_4$ and PbI_2 domains, respectively, convert into 2D $(PEA)_2(MA)_{n-1}Pb_nI_{3n+1}$-layered and 3D $MAPbI_3$ perovskites. It is noted that multiphase of 2D $(PEA)_2(MA)_{n-1}Pb_nI_{3n+1}$ perovskite with n = 1, 2, 3, and 5 along with 3D $MAPbI_3$ nanoplate is simultaneously formed for PEAI/PbI_2 = 1. When the PbI_2 content increases in the precursor, the 3D $MAPbI_3$ nanoplate grows to form $MAPbI_3$ grain, while the multi-2D perovskites are deteriorated into single phase of $(PEA)_2(MA)_{n-1}Pb_nI_{3n+1}$ perovskite with increasing n value. Further reduction of PEAI content in the PEAI/PbI_2 = 0.05 case leads to the $(PEA)_2(MA)_{n-1}Pb_nI_{3n+1}$ perovskite with high n value crystallization with tiny island around the $MAPbI_3$ grain boundary.

The trace existence of PEAI in the perovskite films is confirmed and characterized by Fourier transform infrared (FTIR) spectra and NEXAFS. Figure S4 (Supporting Information) shows the FTIR spectra of spin-coated PEAI-doped PbI_2 films with

© 2018 WILEY-VCH Verlag GmbH & Co. KGaA, Weinheim

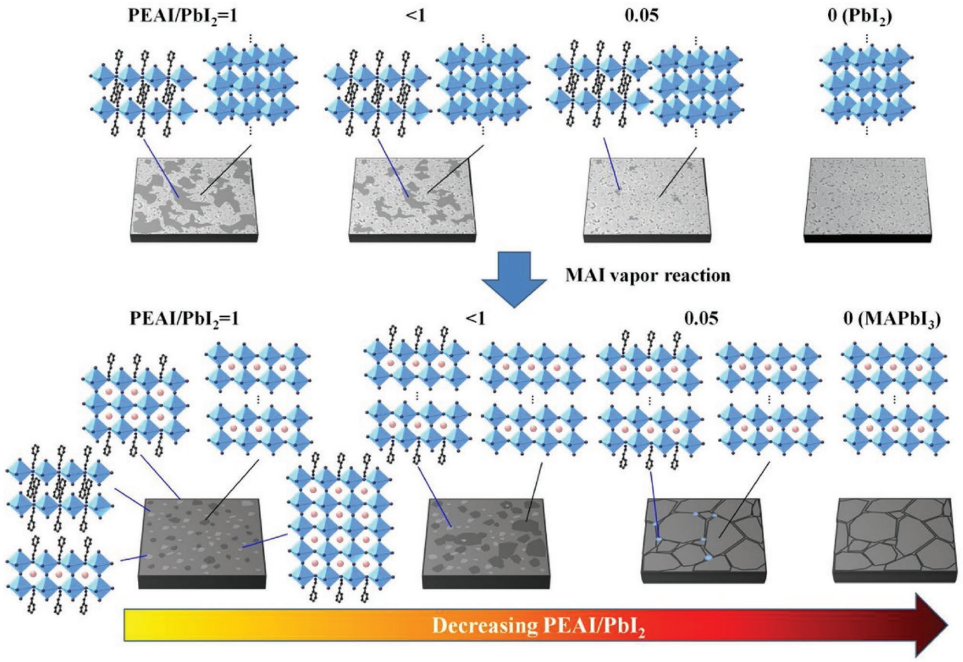

Scheme 1. Composition evolution of 2D and 3D perovskite in the as-fabricated film with variant doping levels of $PEAI/PbI_2$.

variant doping levels and their spectra after vapor treatment. Characteristics peak at 1470 cm^{-1} is responsible for C=C bond from the benzene ring of PEAI, whereas C—H bond of MAI or PEAI displays a feature peak at 1570 cm^{-1}. In Figure S4a (Supporting Information), before vapor treatment, the as-deposited film with high PEAI content ($PEAI/PbI_2$ = 2, 1, and 0.67) displays two feature peaks at 1470 and 1570 cm^{-1}. On the contrary, feature peaks of 1470 and 1570 cm^{-1} disappear when the predominated domain is PbI_2 for the cases of $PEAI/PbI_2$ = 0.1, 0.05, and 0. Figure S4b (Supporting Information) presents the FTIR spectra of PEAI-doped perovskite after vapor reaction for $PEAI/PbI_2$ = 1, 0.67, 0.1, 0.05, and 0. Only one characteristic peak of 1570 cm^{-1} is detected, indicative of the predominated domain of 3D $MAPbI_3$. Since FTIR is a surface sensitive technique, the content of PEA^+ residual in the bulk is hardly detected. By using the scanning transmission X-ray microscopy beamline BL4U at UVSOR Synchrotron, we have successfully confirmed the existence of PEA^+ in the as-fabricated film with the NEXAFS in the bulk-sensitive transmission mode. **Figure 6** presents the spectra of carbon K-edge for perovskite film with $PEAI/PbI_2$ = 2 ($(PEA)_2Pb_1I_4$), 0.05 (with/without MAI vapor treatment), and 0 ($MAPbI_3$) that are covered on the mp-TiO_2-coated SiN membranes. The 2D $(PEA)_2Pb_1I_4$ perovskite exhibits the NEXAFS characteristic peaks at ≈285, ≈287.5, ≈289, ≈293.5, and ≈301.5 eV that are, respectively, assigned as the π^* resonance (photoabsorption transition from C 1s to e_{2u} orbital), Rydberg resonance, 2nd π^* resonance (transition from C 1s to e_{b2g} orbital), and two σ^* resonances (transition from C 1s to e_{1u} and e_{2g} + a_{2g}) of the $C_6H_5(CH_2)_2NH_3^+$ (PEA^+) molecule.[38] When the PEAI is doped in the PbI_2 film for $PEAI/PbI_2$ = 0.05 without vapor reaction, the energy spectral profile along with characteristic peaks is similar to 2D $(PEA)_2Pb_1I_4$ perovskite, suggesting the PEA^+ intercalation in PbI_2 film at the pretreatment stage. After the MAI vapor reaction, the perovskite film with $PEAI/PbI_2$ = 0.05 via LP-VASP presents two characteristic peaks at ≈288.5 and ≈290 eV that are ascribed to the σ^* resonance of C—H and C—N of $CH_3NH_3^+$ (MA^+) cation.[39] The remaining small characteristic peaks around 285 and 301.5 eV of PEA^+ (corresponding to the π^* resonance of C=C bond and σ^* resonance of C=C bond, respectively) imply the intercalation of PEA^+ after the MAI post-treatment.

We examine the composition of perovskite films with different PEAI doping levels by energy dispersive spectroscopy (EDS) analysis and the results are summarized in Table S1 (Supporting Information). The atomic ratio of N/Pb of $(PEA)_2PbI_4$ 2D perovskite is lower than the stoichiometry of

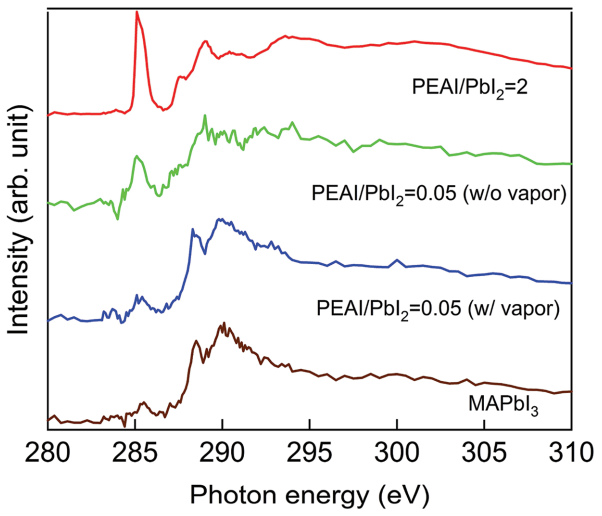

Figure 6. The NEXAFS spectra of carbon K-edge for perovskite film made of $PEAI/PbI_2$ = 2, 0.05 (before MAI vapor reaction), 0.05 (after MAI vapor reaction), and 0 ($MAPbI_3$) films for comparison.

© 2018 WILEY-VCH Verlag GmbH & Co. KGaA, Weinheim

Table 1. The photovoltaic parameters of solar cells using perovskite with variant doping levels in the precursor solution.

$PEAI/PbI_2$	V_{OC} [V]	J_{SC} [mA cm^{-2}]	FF [%]	PCE [%]
0	1.04	21.03	79.05	17.31
0.03	1.06	21.10	83.32	18.69
0.05	1.08	21.91	80.36	19.10
0.1	1.07	18.09	76.43	14.74
0.4	1.02	17.77	75.94	13.80
0.5	1.03	18.63	67.68	13.01
0.67	1.07	18.40	71.03	13.97
1	0.84	9.61	72.08	5.85
2	0.87	0.07	25.38	0.02

precursor, while that of I/Pb is greater than 4, which implies that some excess Pb and I_2 residual might be presented in the spin-coated film. With increasing PbI_2 in the precursor for $PEAI/PbI_2$ = 1, 0.5, 0.1, and 0.05, the N/Pb and I/Pb atomic ratio gradually decreases to ≈1 and 3, which suggested the decrease of 2D domain while the 3D domain dominates. Moreover, N/Pb atomic ratio of ≈1 indicates that the composition of resultant perovskite for $PEAI/PbI_2$ = 0.05 is mainly dominated by $MAPbI_3$ which corresponds to what we have observed in the XRD and GIWAXS results. The relatively higher value of N/Pb and I/Pb in $MAPbI_3$ film indicates some MAI residual from the vapor on the perovskite surface.

To explore the role of PEAI with different doping levels on the photovoltaic performance, the device configuration of fluorine-doped tin oxide (FTO)/compact TiO_2/mesoporous TiO_2/perovskite/2,2,7,7-tetrakis(N,N-di-p-methoxyphenylamine)-9,9-spirobifluorene (spiro-OMeTAD)/Ag is fabricated with their photovoltaic characteristics are listed in **Table 1**. **Figure 7**a plots the statistic device efficiency under reverse scan direction (1.2 to −0.2 V) as a function of doping level, and the maximum efficiency of 19.10% is achieved for the device made of $PEAI/PbI_2$ = 0.05 mainly due to enhanced V_{OC} and FF. As analyzed from the UV–vis, PL, XRD, and GIWAXS results, the vapor-treated PEAI-doped perovskite has dimensionality evolution with variant PEAI contents. The device composed of layered $(PEA)_2PbI_4$ perovskite exhibits extremely low efficiency of 0.02% because the high exciton binding energy in the 2D structure prohibits the separation of electron–hole pair. Moreover, the thickness of spin-coated film is over 700 nm owing to high viscosity of precursor that hampers the carrier extraction by the electrode. For perovskite solar cell made of $PEAI/PbI_2$ = 1, the 2D/3D hybrid device delivers an increased J_{SC} of 9.61 mA cm^{-2} to improve the overall efficiency to 5.85%, whose *J*–*V* curve and photovoltaic parameters are shown in Figure S5a (Supporting Information). Owing to the coexisted 3D $MAPbI_3$ structure, the absorption extending to ≈780 nm

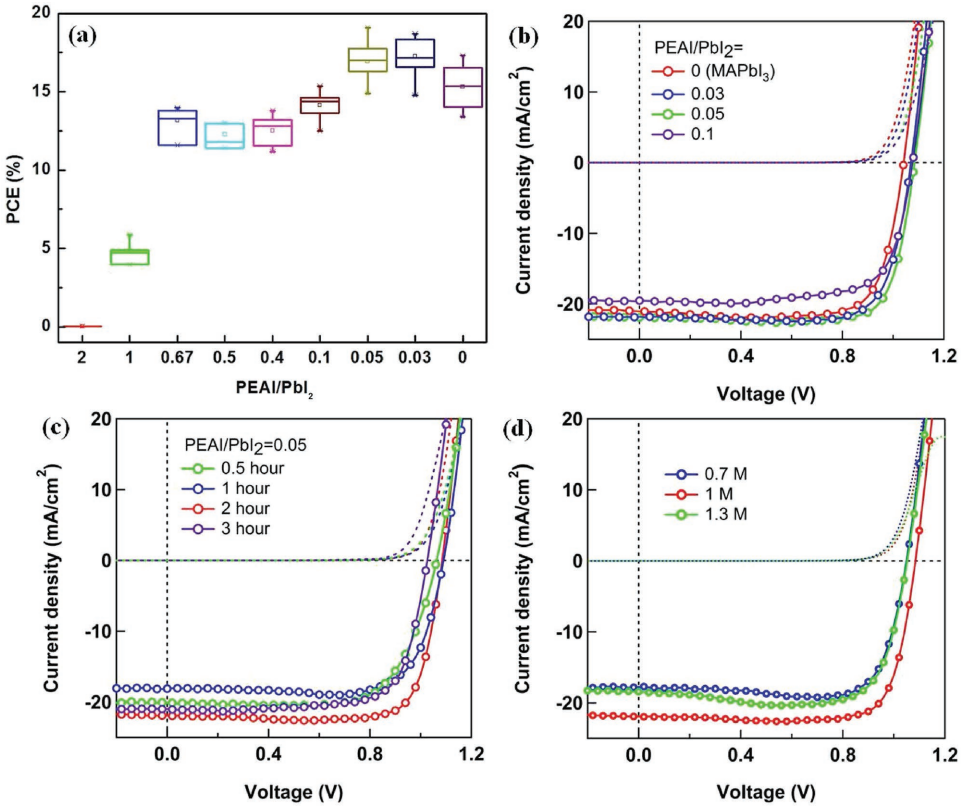

Figure 7. a) The statistic power conversion efficiency of perovskite solar cells made with variant doping levels of $PEAI/PbI_2$. b) The *J*–*V* curves of perovskite solar cells with $PEAI/PbI_2$ = 0.1, 0.05, 0.03, and 0. c,d) The *J*–*V* curves of devices made with $PEAI/PbI_2$ = 0.05 for reaction time from 0.5, 1.0, 2 to 3 h (c) and concentration of PEAI-doped PbI_2 precursor of 0.7, 1.0, and 1.3 M with a reaction time of 2 h (d).

© 2018 WILEY-VCH Verlag GmbH & Co. KGaA, Weinheim

improves the light harvesting capability and the amount of photoexcited carriers. However, the multiphase of 2D-layered structure hinders the carrier transport, and therefore, fewer free carriers could be collected by the contact electrode. A significant enhancement on photocurrent along with efficiency is achieved for device made with PEAI/PbI_2 = 0.67, 0.5, and 0.4. The increasing PbI_2 content raises the 3D $MAPbI_3$ domain in the perovskite film which further enhances the light harvesting and facilitates the free carrier transport. Figure 7b presents the *J*–*V* curves of PEAI-doped perovskite solar cells with PEAI/PbI_2 = 0.1, 0.05, and 0.03, compared with the counterpart prepared with PEAI/PbI_2 = 0. When the ratio of PEAI/PbI_2 is below 0.5, the vapor-treated perovskite films mainly composed of 3D $MAPbI_3$ structure as proven from the XRD and GIWAX results. The device employing perovskite with PEAI/PbI_2 = 0.05 shows the champion efficiency of 19.10% mainly due to the enhanced J_{SC} and V_{OC} as compared to the counterparts with PEAI/PbI_2 = 0.1, 0.03, and 0. From the KPFM results, the perovskite film with PEAI/PbI_2 = 0.05 exhibits a higher surface potential and the device voltage is thus improved. The SEM results indicate that tiny dopant of PEAI in the perovskite for PEAI/PbI_2 = 0.05 improves the grain size and promotes the preferred orientation of crystalline facet (310) instead of (110) facet which facilitates the carrier transport.[32] Figure S6 (Supporting Information) shows the cross-sectional SEM image of fabricated perovskite solar cells with PEAI/PbI_2 = 0.05. We observe single perovskite grain across two selective contacts with a thickness of ≈550 nm, which allowed saturated light absorption and incident photon-to-electron conversion efficiency (IPCE) in the red-light range, as displayed in Figure S5b (Supporting Information). The *J*–*V* curves of the perovskite solar cells made of PEAI/PbI_2 = 0.05 and 0 ($MAPbI_3$) with forward (from –0.2 to 1.2 V) and reverse (from 1.2 to –0.2 V) scan directions as well as difference scan rate are shown in Figure S7a,b (Supporting Information). It is clear that the perovskite solar cells with PEAI/PbI_2 = 0.05 exhibit less hysteresis than the $MAPbI_3$-based device under similar scan rate, indicating that appropriate PEAI dopant can suppress the hysteresis effect. However, for both devices, the scan rate dependent *J*–*V* curves imply the existence of capacitive hysteresis from interface charge accumulation.[40] Figure S7c,d (Supporting Information) shows *J*–*V* curves of forward and reverse scan directions for the devices made of different PEAI doping levels with a constant scan rate of 0.14 V s^{-1}. A hysteresis index (HI) defined as HI = $[P_{max,r}/P_{max,f}] - 1$, where $P_{max,r}$ is the maximum power point on the reverse scan and $P_{max,f}$ is the maximum power point on the forward scan, is applied to estimate the extent of hysteresis.[41] The HI for devices of different doping levels is summarized in Table S2 (Supporting Information). The hysteresis can be reduced with the increasing of PEAI dopant, suggesting that the existence of 2D perovskite can suppress the hysteresis either by impeding ion migration or by passivation of $MAPbI_3$.

The reaction time and precursor concentration have influences on the synthesized perovskite crystallization and the resultant photovoltaic performances. PEAI-doped perovskite for PEAI/PbI_2 = 0.05 with different reaction times is conducted to further improve the device performance, whose *J*–*V* curve and IPCE spectra are, respectively, shown in Figure 7c and Figure S8a (Supporting Information). The perovskite-based perovskite solar cell made of PEAI/PbI_2 = 0.05 with a reaction time of 2 h delivers the highest efficiency of 19.10% compared to the devices with reaction time of 0.5, 1, and 3 h, mainly due to the enhanced J_{SC} and superior FF. It is noted that a plateau of IPCE response over 80% across 400–750 nm, revealing the high photon-to-electron conversion efficiency of the fabricated device. By fine-tuning the concentration of PEAI-doped PbI_2 precursor, the thickness of perovskite could be controlled to optimize the device performance in terms of *J*–*V* curves and IPCE response depicted in Figure 7d and Figure S8b (Supporting Information), respectively. The absorption spectra, XRD, and SEM images of perovskite made of 0.7, 1.0, and 1.3 M are shown in Figure S8c–h (Supporting Information). After the MAI vapor reaction, the absorption of perovskite for 0.7 M shown in Figure S8c (Supporting Information) presents a lower absorption response, which results in a lower photocurrent of 17.76 mA cm^{-2} for the solar cell compared to the device made of 1.0 M. When the concentration reaches 1.0 M, an enhanced absorption improves light harvesting capability as well as photocurrent for the device. With further increase of concentration to 1.3 M, the absorption in long wavelength range (530–780 nm) can be further enhanced because the increased thickness over 700 nm of perovskite improves the light harvesting capability in such wavelength range (Figure S8h, Supporting Information). However, the 1.3 M-based devices achieve a lower power conversion efficiency that is attributed to the decreased photocurrent. The active layer may be too thick, which leads to carrier recombination before charge collection and is responsible for the decreased photocurrent of devices. The photovoltaic parameters of devices with variant reaction times and concentrations are summarized in Table S3 (Supporting Information). The stability tests for four encapsulated devices made of PEAI/PbI_2 = 0.05 and 0 ($MAPbI_3$) under one sun light soaking (100 mW cm^{-2}) are conducted and the results are shown in Figure S9a (Supporting Information). Figure S9b (Supporting Information) shows the averaged PCE evolution by four devices corresponding to $MAPbI_3$- and PEAI-doped cells. The PEAI-doped devices maintained over 60% of initial PCE after light soaking for 140 h which is superior than the $MAPbI_3$ counterpart, demonstrating that the durable 2D/3D hybrid perovskite effectively enhanced the device stability. However, the degradation can be resulted from the application of organic hole transport layer of spiro-OMeTAD, which is not the best candidate for long-term stability. Nevertheless, it is obvious that the PEAI-doped perovskite demonstrated better stability than pure $MAPbI_3$ in the control experiment.

In conclusion, we employ low-pressure vapor-assisted solution process to fabricate 2D/3D hybrid perovskite with different doping levels of PEAI/PbI_2. With reduction of PEAI/PbI_2 from 2 to 0, the dimensionality of the as-fabricated perovskite film evolves from 2D, hybrid 2D/3D to 3D structure. XRD, GIWAXS, SEM, and KPFM are conducted to realize the crystallization evolution of the perovskite film with different doping levels of PEAI/PbI_2, suggesting that the PEA^+-intercalated perovskite with high *n* value is crystallized around $MAPbI_3$ grain to improve the $MAPbI_3$ grain growth. A remarkable power conversion efficiency of 19.10% is demonstrated for 2D/3D hybrid perovskite solar cells with PEAI/PbI_2 = 0.05 due to the PEAI-modified perovskite grain size and surface potential.

© 2018 WILEY-VCH Verlag GmbH & Co. KGaA, Weinheim

Supporting Information

Supporting Information is available from the Wiley Online Library or from the author.

Acknowledgements

The authors are grateful to the research grant from the Ministry of Science and Technology (MOST 106-2119-M-006-017, MOST 106-2811-M-006-046, MOST 106-2119-M-006-027, and MOST 106-2119-M-006-004). P.C. thanks the financial support from the Top-Notch Project under the Headquarter of University Advancement at the National Cheng Kung University, which is sponsored by the Ministry of Education, Taiwan, ROC. The funding from the Research Center for Energy Technology and Strategy (RCETS) and the Advanced Optoelectronic Technology Center (AOTC), National Cheng Kung University is acknowledged. The authors thank the assistance from Dr. Shu-Ju Tsai and Wei-Ching Guo (CMNST, NCKU) for the KPFM experiments. This work was financially supported by the Hierarchical Green-Energy Materials (Hi-GEM) Research Center, from The Featured Areas Research Center Program within the framework of the Higher Education Sprout Project by the Ministry of Education (MOE) in Taiwan.

Conflict of Interest

The authors declare no conflict of interest.

Keywords

2D/3D hybrid perovskites, low-temperature vapor-assisted solution processing, perovskite solar cells, Ruddlesden–Popper perovskites

Received: March 2, 2018
Revised: April 14, 2018
Published online:

[1] a) J.-P. Correa-Baena, A. Abate, M. Saliba, W. Tress, T. Jesper Jacobsson, M. Gratzel, A. Hagfeldt, *Energy Environ. Sci.* **2017**, *10*, 710; b) H. Wang, D. H. Kim, *Chem. Soc. Rev.* **2017**, *46*, 5204; c) J. Zhang, X. Yang, H. Deng, K. Qiao, U. Farooq, M. Ishaq, F. Yi, H. Liu, J. Tang, H. Song, *Nano-Micro Lett.* **2017**, *9*, 36; d) S. A. Veldhuis, P. P. Boix, N. Yantara, M. Li, T. C. Sum, N. Mathews, S. G. Mhaisalkar, *Adv. Mater.* **2016**, *28*, 6804.

[2] M. M. Lee, J. Teuscher, T. Miyasaka, T. N. Murakami, H. J. Snaith, *Science* **2012**, *338*, 643.

[3] a) M. B. Johnston, L. M. Herz, *Acc. Chem. Res.* **2016**, *49*, 146; b) L. M. Herz, *Annu. Rev. Phys. Chem.* **2016**, *67*, 65.

[4] a) A. Kojima, K. Teshima, Y. Shirai, T. Miyasaka, *J. Am. Chem. Soc.* **2009**, *131*, 6050; b) M. Saliba, T. Matsui, J.-Y. Seo, K. Domanski, J.-P. Correa-Baena, M. K. Nazeeruddin, S. M. Zakeeruddin, W. Tress, A. Abate, A. Hagfeldt, M. Gratzel, *Energy Environ. Sci.* **2016**, *9*, 1989; c) G. E. Eperon, S. D. Stranks, C. Menelaou, M. B. Johnston, L. M. Herz, H. J. Snaith, *Energy Environ. Sci.* **2014**, *7*, 982.

[5] G. Niu, X. Guo, L. Wang, *J. Mater. Chem. A* **2015**, *3*, 8970.

[6] A. M. Ganose, C. N. Savory, D. O. Scanlon, *Chem. Commun.* **2017**, *53*, 20.

[7] a) C. C. Stoumpos, D. H. Cao, D. J. Clark, J. Young, J. M. Rondinelli, J. I. Jang, J. T. Hupp, M. G. Kanatzidis, *Chem. Mater.* **2016**, *28*, 2852; b) J.-C. Blancon, H. Tsai, W. Nie, C. C. Stoumpos, L. Pedesseau, C. Katan, M. Kepenekian, C. M. M. Soe, K. Appavoo, M. Y. Sfeir, S. Tretiak, P. M. Ajayan, M. G. Kanatzidis, J. Even, J. J. Crochet, A. D. Mohite, *Science* **2017**, *355*, 1288; c) S. Ahmad, X. Guo, *Chin. Chem. Lett.* **2018**, *29*, 657; d) R. K. Misra, B.-E. Cohen, L. Iagher, L. Etgar, *ChemSusChem* **2017**, *10*, 3712; e) P. Chen, Y. Bai, M. Lyu, J.-H. Yun, M. Hao, L. Wang, *Sol. RRL* **2018**, *2*, 1700186; f) F. Xu, T. Zhang, G. Li, Y. Zhao, *J. Mater. Chem. A* **2017**, *5*, 11450.

[8] X. Gan, O. Wang, K. Liu, X. Du, L. Guo, H. Liu, *Sol. Energy Mater. Sol. Cells* **2017**, *162*, 93.

[9] C. C. Stoumpos, C. M. M. Soe, H. Tsai, W. Nie, J.-C. Blancon, D. H. Cao, F. Liu, B. Traoré, C. Katan, J. Even, A. D. Mohite, M. G. Kanatzidis, *Chem* **2017**, *2*, 427.

[10] I. C. Smith, E. T. Hoke, D. Solis-Ibarra, M. D. McGehee, H. I. Karunadasa, *Angew. Chem., Int. Ed.* **2014**, *53*, 11232.

[11] M.-H. Jung, *Electrochim. Acta* **2017**, *240*, 98.

[12] G. Grancini, C. Roldán-Carmona, I. Zimmermann, D. Martineau, S. Narbey, F. Oswald, M. K. Nazeeruddin, *Mesoscale Nanoscale Phys.* **2016**, arXiv:1609.09846.

[13] a) K. Yao, X. Wang, Y.-x. Xu, F. Li, L. Zhou, *Chem. Mater.* **2016**, *28*, 3131; b) K. Yao, X. Wang, F. Li, L. Zhou, *Chem. Commun.* **2015**, *51*, 15430.

[14] a) L. Junze, W. Jun, Z. Yingjun, W. Haizhen, L. Gaoming, X. Xuan, Z. Weihang, L. Hongmei, L. Dehui, *2D Mater.* **2018**, *5*, 021001; b) L. Li, Z. Sun, P. Wang, W. Hu, S. Wang, C. Ji, M. Hong, J. Luo, *Angew. Chem., Int. Ed.* **2017**, *56*, 12150.

[15] C. Ma, C. Leng, Y. Ji, X. Wei, K. Sun, L. Tang, J. Yang, W. Luo, C. Li, Y. Deng, S. Feng, J. Shen, S. Lu, C. Du, H. Shi, *Nanoscale* **2016**, *8*, 18309.

[16] D. Yu, B. Cai, F. Cao, X. Li, X. Liu, Y. Zhu, J. Ji, Y. Gu, H. Zeng, *Adv. Mater. Interfaces* **2017**, *4*, 1700441.

[17] G. Grancini, C. Roldán-Carmona, I. Zimmermann, E. Mosconi, X. Lee, D. Martineau, S. Narbey, F. Oswald, F. De Angelis, M. Graetzel, M. K. Nazeeruddin, *Nat. Commun.* **2017**, *8*, 15684.

[18] J. Chen, J.-Y. Seo, N.-G. Park, *Adv. Energy Mater.* **2018**, *8*, 1702714.

[19] L. N. Quan, M. Yuan, R. Comin, O. Voznyy, E. M. Beauregard, S. Hoogland, A. Buin, A. R. Kirmani, K. Zhao, A. Amassian, D. H. Kim, E. H. Sargent, *J. Am. Chem. Soc.* **2016**, *138*, 2649.

[20] B.-E. Cohen, M. Wierzbowska, L. Etgar, *Adv. Funct. Mater.* **2017**, *27*, 1604733.

[21] D. H. Cao, C. C. Stoumpos, O. K. Farha, J. T. Hupp, M. G. Kanatzidis, *J. Am. Chem. Soc.* **2015**, *137*, 7843.

[22] H. Tsai, W. Nie, J.-C. Blancon, C. C. Stoumpos, R. Asadpour, B. Harutyunyan, A. J. Neukirch, R. Verduzco, J. J. Crochet, S. Tretiak, L. Pedesseau, J. Even, M. A. Alam, G. Gupta, J. Lou, P. M. Ajayan, M. J. Bedzyk, M. G. Kanatzidis, A. D. Mohite, *Nature* **2016**, *536*, 312.

[23] X. Zhang, X. Ren, B. Liu, R. Munir, X. Zhu, D. Yang, J. Li, Y. Liu, D.-M. Smilgies, R. Li, Z. Yang, T. Niu, X. Wang, A. Amassian, K. Zhao, S. Liu, *Energy Environ. Sci.* **2017**, *10*, 2095.

[24] Z. Wang, Q. Lin, F. P. Chmiel, N. Sakai, L. M. Herz, H. J. Snaith, *Nat. Energy* **2017**, *2*, 17135.

[25] a) J.-F. Liao, H.-S. Rao, B.-X. Chen, D.-B. Kuang, C.-Y. Su, *J. Mater. Chem. A* **2017**, *5*, 2066; b) T. Zhang, M. I. Dar, G. Li, F. Xu, N. Guo, M. Grätzel, Y. Zhao, *Sci. Adv.* **2017**, *3*, e1700841.

[26] Y. Lin, Y. Bai, Y. Fang, Z. Chen, S. Yang, X. Zheng, S. Tang, Y. Liu, J. Zhao, J. Huang, *J. Phys. Chem. Lett.* **2018**, *9*, 654.

[27] a) F. Giustino, H. J. Snaith, *ACS Energy Lett.* **2016**, *1*, 1233; b) M. Lyu, J.-H. Yun, P. Chen, M. Hao, L. Wang, *Adv. Energy Mater.* **2017**, *7*, 1602512; c) H. Hu, B. Dong, W. Zhang, *J. Mater. Chem. A* **2017**, *5*, 11436; d) Z. Shi, J. Guo, Y. Chen, Q. Li, Y. Pan, H. Zhang, Y. Xia, W. Huang, *Adv. Mater.* **2017**, *29*, 1605005.

[28] D. H. Cao, C. C. Stoumpos, T. Yokoyama, J. L. Logsdon, T.-B. Song, O. K. Farha, M. R. Wasielewski, J. T. Hupp, M. G. Kanatzidis, *ACS Energy Lett.* **2017**, *2*, 982.

[29] Y. Liao, H. Liu, W. Zhou, D. Yang, Y. Shang, Z. Shi, B. Li, X. Jiang, L. Zhang, L. N. Quan, R. Quintero-Bermudez, B. R. Sutherland, Q. Mi, E. H. Sargent, Z. Ning, *J. Am. Chem. Soc.* **2017**, *139*, 6693.

© 2018 WILEY-VCH Verlag GmbH & Co. KGaA, Weinheim

[30] S. Shao, J. Liu, G. Portale, H.-H. Fang, G. R. Blake, G. H. ten Brink, L. J. A. Koster, M. A. Loi, *Adv. Energy Mater.* **2017**, *8*, 1702019.
[31] a) P.-S. Shen, Y.-H. Chiang, M.-H. Li, T.-F. Guo, P. Chen, *APL Mater.* **2016**, *4*, 091509; b) L. K. Ono, M. R. Leyden, S. Wang, Y. Qi, *J. Mater. Chem. A* **2016**, *4*, 6693.
[32] P.-S. Shen, J.-S. Chen, Y.-H. Chiang, M.-H. Li, T.-F. Guo, P. Chen, *Adv. Mater. Interfaces* **2016**, *3*, 1500849.
[33] Y.-H. Chiang, H.-M. Cheng, M.-H. Li, T.-F. Guo, P. Chen, *ChemSusChem* **2016**, *9*, 2620.
[34] S.-S. Li, C.-H. Chang, Y.-C. Wang, C.-W. Lin, D.-Y. Wang, J.-C. Lin, C.-C. Chen, H.-S. Sheu, H.-C. Chia, W.-R. Wu, U. S. Jeng, C.-T. Liang, R. Sankar, F.-C. Chou, C.-W. Chen, *Energy Environ. Sci.* **2016**, *9*, 1282.
[35] H.-C. Chia, H.-S. Sheu, Y.-Y. Hsiao, S.-S. Li, Y.-K. Lan, C.-Y. Lin, J.-W. Chang, Y.-C. Kuo, C.-H. Chen, S.-C. Weng, C.-J. Su, A.-C. Su, C.-W. Chen, U. S. Jeng, *ACS Appl. Mater. Interfaces* **2017**, *9*, 36897.
[36] W. Peng, J. Yin, K.-T. Ho, O. Ouellette, M. De Bastiani, B. Murali, O. El Tall, C. Shen, X. Miao, J. Pan, E. Alarousu, J.-H. He, B. S. Ooi, O. F. Mohammed, E. Sargent, O. M. Bakr, *Nano Lett.* **2017**, *17*, 4759.
[37] Y.-H. Chiang, M.-H. Li, H.-M. Cheng, P.-S. Shen, P. Chen, *ACS Appl. Mater. Interfaces* **2017**, *9*, 2403.
[38] a) K. Weiss, S. Gebert, M. Wühn, H. Wadepohl, C. Wöll, *J. Vac. Sci. Technol., A* **1998**, *16*, 1017; b) Y. Joseph, M. Wuhn, A. Niklewski, W. Ranke, W. Weiss, C. Woll, R. Schlogl, *Phys. Chem. Chem. Phys.* **2000**, *2*, 5314.
[39] a) W. Huang, F. Huang, E. Gann, Y.-B. Cheng, C. R. McNeill, *Adv. Funct. Mater.* **2015**, *25*, 5529; b) N.-K. Kim, Y. H. Min, S. Noh, E. Cho, G. Jeong, M. Joo, S.-W. Ahn, J. S. Lee, S. Kim, K. Ihm, H. Ahn, Y. Kang, H.-S. Lee, D. Kim, *Sci. Rep.* **2017**, *7*, 4645; c) M.-C. Jung, Y. M. Lee, H.-K. Lee, J. Park, S. R. Raga, L. K. Ono, S. Wang, M. R. Leyden, B. D. Yu, S. Hong, Y. Qi, *Appl. Phys. Lett.* **2016**, *108*, 073901.
[40] a) P. Lopez-Varo, J. A. Jiménez-Tejada, M. García-Rosell, S. Ravishankar, G. Garcia-Belmonte, J. Bisquert, O. Almora, *Adv. Energy Mater.* **2018**, *8*, 1702772; b) B. Chen, M. Yang, S. Priya, K. Zhu, *The Journal of Phys. Chem. Lett.* **2016**, *7*, 905.
[41] P. Calado, A. M. Telford, D. Bryant, X. Li, J. Nelson, B. C. O'Regan, P. R. F. Barnes, *Nat. Commun.* **2016**, *7*, 13831.

© 2018 WILEY-VCH Verlag GmbH & Co. KGaA, Weinheim